*Published in Journal of Thermophysics and Heat Transfer (AIAA)* *April, 2014*

# Thermal-Fluid Modeling for High Thermal Conductivity Heat Pipe Thermal Ground Planes


| **Mohammed T. Ababneh**[1] | **Frank M. Gerner** | **Pramod Chamarthy** |
|---|---|---|
| University of Cincinnati | University of Cincinnati | CoolChip Technologies |
| Cincinnati, Ohio, USA | Cincinnati, Ohio, USA | Boston, Massachusetts, USA |
| **Peter de Bock** | **Shakti Chauhan** | **Tao Deng** |
| GE Global Research Center | GE Global Research Center | Shanghai Jiao Tong University |
| Niskayuna, New York, USA | Niskayuna, New York, USA | Shanghai, China |



## ABSTRACT

**The thermal ground plane (TGP) is an advanced planar heat pipe designed for cooling microelectronics in high gravitational fields. A thermal resistance model is developed to predict the thermal performance of the TGP, including the effects of the presence of non-condensable gases (NCGs). Viscous laminar flow pressure losses are predicted to determine the maximum heat load when the capillary limit is reached. This paper shows that the axial effective thermal conductivity of the TGP decreases when the substrate and/or wick are thicker and/or with the presence of NCGs. Moreover, it was demonstrated that the thermal-fluid model may be utilized to optimize the performance of the TGP by estimating the limits of wick thickness and vapor space thickness for a recognized internal volume of the TGP. The wick porosity plays a significant role on maximum heat transport capability. A large adverse gravitational field strongly decreases the maximum heat transport capability of the TGP. Axial effective thermal conductivity is mostly unaffected by the gravitational field. The maximum length of the TGP before reaching the capillary limit is inversely proportional to input power.**



[1] **The corresponding author currently R&D Engineer, Defense/Aerospace Division, Advanced Cooling Technologies, Inc., Lancaster, PA 17601; E-mail: mohammed.ababneh@1-act.com**

## NOMENCLATURE

| | | | |
|---|---|---|---|
| A | area [$m^2$]. | $\dot{m}$ | mass flow rate [kg/s]. |
| AlN | Aluminum nitride. | NCGs | non-condensable gases. |
| Bi | Biot number. | $Q_{HP}$ | heat load for the heat pipe [W]. |
| $C_1$ | Empirical value related to the contact angle and the standard deviation of average pore diameter. | $Q_{in}$ | input power [W]. |
| | | $Q_{max}$ | maximum heat transport capability [W]. |
| Csf | Shape factor. | R | Thermal Resistance [℃/W] |
| CTE | coefficient of thermal expansion. | $r_{pore}$ | pore radius [µm]. |
| $d_{pore}$ | pore diameter [µm]. | s | solid. |
| EES | engineering equation solver. | t | Thickness [m]. |
| f | the ratio of blockage. | T | Temperature [℃]. |
| g | gravitational acceleration [$m/s^2$]. | TGPs | thermal ground planes. |
| h | heat transfer coefficient [$W/m^2.K$] | $V_{ncgs}$ | volume occupied by non-condensable gases. |
| $h_{fg}$ | latent heat of evaporation [J/kg]. | $V_{total}$ | total volume inside the TGP. |
| Ja | Jacob number, $Ja=\rho_l C_p(T_w-T_{sat})/(\rho_v h_{fg})$. | $y_{ncgs}$ | mole fraction of non-condensable gases. |
| K | permeability [$m^2$]. | ε | porosity[-]. |
| $k_{eff}$ | axial effective thermal conductivity [W/m.K]. | µ | dynamic viscosity [Pa.s]. |
| L | length [m]. | ρ | density [kg/m3]. |
| l | liquid. | σ | surface tension [N/m]. |

## INTRODUCTION

Heat pipes operate in a broad variety of heat transfer related applications where high power and low temperature drops are required. Flat heat pipes are an efficient technology for spacecraft cooling and electronic cooling applications due to their high thermal conductivity, low weight, and reliability [1]. For a heat pipe to work appropriately, the net capillary pressure difference between wet and dry pressures points must be greater than the sum of pressure losses in the system. Heat pipe performance is typically constrained by the flow resistance of the wick, which limits mass flow and the total heat load the system is able to transport. If the heat load on a heat pipe is increased, the mass flow inside the device increases. As the axial pressure gradient of the liquid within the wick structure increases, a point is reached where the capillary pressure difference across the vapor-liquid interface in the evaporator equals the total

pressure losses in the system. The maximum heat transport of the device is reached at this point. So if the heat load exceeds this point, the wick will dry out in the evaporator region and the heat pipe will not work. This point is called the capillary limit [2].

Thermal ground planes (TGPs) are flat thin (about 3 mm thick) heat pipes which utilize two-phase cooling as in common heat pipes. Major advantages, however, include the ability to integrate directly with the microelectronic substrate for a wide range of applications due to the substrate being made out of material that is CTE-matched with common semiconductor materials such as Si, SiGe, AlN and SiC, so Copper and aluminum nitride (AlN) are selected to meet the CTE mismatch requirement. Advantages of the TGP, as well as other heat pipes, include a very high effective axial thermal conductivity, reliability, no moving parts, and no need for external power. Unlike conventional heat pipes, the TGP can be used in applications where space is extremely limited and it can operate in high-g environments. Figure 1 shows TGP which is a thin planar heat spreader that is capable of moving heat from multiple chips to a distant thermal sink. The aim is to use TGPs as thermal spreader in a variety of microelectronic cooling applications. These TGPs will perform as a new generation of high-performance, integrated systems to operate at a high power density with a reduced temperature gradient and weight. In addition to being able to dissipate large amounts of heat, they have very high effective thermal conductivities and (because of nano-porous wicks) can operate in high adverse gravitational fields. Since the TGP utilizes the transport of the latent energy from the evaporator to the condenser, the TGP has an extremely large effective thermal conductivity. A thermal resistance model is presented in this manuscript which is able to predict the temperatures for a given heat input, with or without the presence of NCGs, which typically accumulate in the condenser section of the TGP. The heat transferred to the evaporator section by an external source is conducted through the TGP wall and wick structure, and then vaporizes the working fluid in the wick. As vapor is formed, its pressure increases, which drives the vapor to the condenser, where the vapor releases its latent heat of vaporization to the heat sink in the condenser. The condensed fluid returns to the evaporator due to a pressure difference. Thus, the heat pipe is able to transport the latent heat of vaporization in the TGP. This process will continue as long as there is sufficient capillary pressure to pull the condensed liquid from the condenser into the evaporator by the surface tension [2-5].

There are numerous experimental, analytical and numerical models have been developed to study the performance of heat pipes. Van Ooijen and Hoogendoorn [6] introduced a steady-state numerical analysis of the vapor core in a horizontal flat heat pipe. A three-dimensional model has been presented to study the hydrodynamic and thermal characteristics of flat heat pipes by Xiao and Faghri [7]. The model includes the heat conduction in the solid wall, fluid flow in the wick region and vapor core, and the coupled heat and mass transfer at the liquid/vapor interface. Zaghdoudi and Sarno [8] studied the effects of body forces environment on the thermal performance of a flat heat pipe using constant heat load. Thomas and Yerkes [9] examined copper/water arterial wick heat pipe with the amplitude of the radial acceleration ranged from 1.1 to 9.8 g. Also, the effects of the dry-out of the heat pipe were tested.

Rice and Faghri [10] introduced a full numerical analysis of heat with no empirical correlations while including the flow in a wick. The capillary pressure required in the wick to drive the flow is attained for several power levels and heating configurations. Sonan et. al. [11] analyzed the transient performance of a flat heat pipe used to cool multiple electronics components by computing the fluid flows in vapor core and wick region using a transient two-dimensional hydrodynamic model. Vadakkan U. et al. [12] solved a transient and steady state performance of a flat heat pipe exposed to heating with multiple discrete heat sources numerically. Momentum and energy equations are solved in the vapor and liquid regions, together with heat conduction in the solid wall. The heat and mass transport at the vapor/liquid interface become more significant as heat pipes decrease in size in order to analyze the performance of heat pipes properly.

The local thermal equilibrium between the solid and liquid phases assumption by using a porous media energy equation is not valid for the present study as assumed in [12]. Since the ratio of solid to liquid thermal conductivities ($k_{\text{sintered copper}} / k_{\text{water}} \approx 275$) is very large [5]. For the TGPs investigated which utilize water as the working fluid, Ja <<1, and convection in the liquid can be neglected. Therefore, the energy transport with the fluid saturated wick is purely by diffusion. Just as important as not having a convection term in the energy equation ($u\ dT/dx \approx 0$), is the assumption that the evaporative heat transfer coefficient ( $h_{evap}$ ) is only a function of temperature. A mass transport experiment (MTE) is utilized to find $h_{evap}$ experimentally in order to estimate the performance of the TGP. For our case, the thin film resistance is much larger than the vertical wick and substrate thermal resistances where the energy transport within the substrate and the vertical wick by conduction. For conventional heat pipes the Bi>>1 because the conduction thermal resistance (t/k.A) is much larger than the convection thermal resistance (1/h.A). For the TGP the conduction resistance was reduced by decreasing the thickness of TGP and by using substrate and wick materials that has relatively high thermal conductivity so Bi ~1 that means the convection resistance or the thin film resistance become more significant.

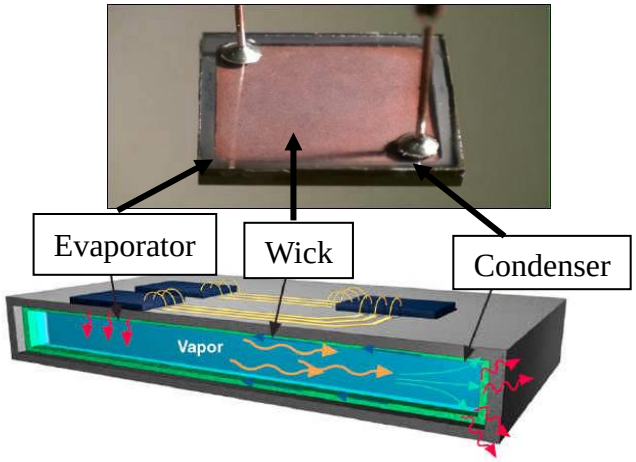


**Figure 1: Engineered nanostructures for high thermal conductivity prototype TGP substrates [13].**

## THEORTICAL MODEL

A thermal resistance model and a pressure drop model are developed which include the major physics governing fluid flow and heat transfer inside the TGP. The thermal resistance model contains a simple pure conduction model and pressure drop models that can consider non-condensable gases (NCGs), which typically accumulate in the condenser section of the TGP. This model is then extended to consider the effect of NCGs on the TGP performance by using a flat front model.

The NCGs present in the heat pipe accumulate in the condenser section and will reduce the performance of the TGP, as shown later in the results. A common assumption is that the gas forms a flat front (vertical shape) across the width of the pipe [14], that any part of the condenser blocked by the gas is stopped proportionally to the obstruction, and that the rate of heat transfer in the condenser degrades proportional to the amount of blockage or (f) value, as shown in Figure 2. For a recognized quantity of gas (given in gm-mole or lb-mole), the length of the blocked part is estimated using the existing saturation pressure corresponding to the temperature of the vapor; (f) is the area fraction which depends on the ratio of NCGs ($y_{ncgs}$) as:

$$f = \left( \frac{L}{L_{Condenser}} \right) y_{ncgs} \qquad (1)$$

Where the ratio of $y_{ncgs}$ is calculated from:

$$y_{ncgs} = \frac{V_{ncgs}}{V_{total}} \qquad (2)$$

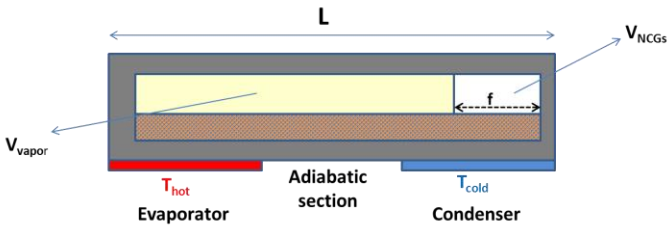


**Figure 2: Schematic of the TGP's cross section.**

One important issue for the designer is the temperature drop between the evaporator and condenser of the TGP. The simplified thermal pathway for the TGP with non-condensable gases is shown in Figure 3.

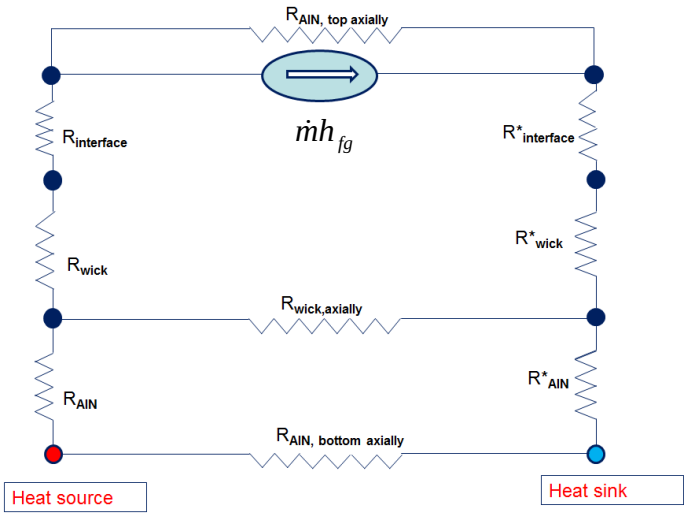


**Figure 3: TGP's thermal pathway.**

The definition of the thermal resistance for the TGP from Figure 3:

Conduction through AlN substrate is:

$$R_{AlN} = \frac{t_{sub}}{k_{sub}.A_{chip}},\ R^*_{AlN} = \frac{t_{sub}}{k_{sub}.(1-f).A_{chip}} \quad (3)$$

Conduction through Wick is:

$$R_{wick} = \frac{t_{wick}}{k_{wick}.A_{chip}},\ R^*_{wick} = \frac{t_{wick}}{k_{wick}.(1-f).A_{chip}} \quad (4)$$

Axial conduction is:

$$R_{AlN,axially} = \frac{L_{sub}}{k_{sub}.A},\ R_{wick,axially} = \frac{L_{wick}}{k_{wick}.A} \quad (5)$$

Thin film resistance at interface is:

$$R_{interface} = \frac{1}{h_{evap}.A_{chip}},\ R^*_{interface} = \frac{1}{h_{cond}.(1-f).A_{chip}} \quad (6)$$

Figure 4 shows the 3D TGP geometry. The length of TGP was varied (3cm, 9cm and 15cm) where the evaporator/condenser length is fixed at 1cm. the width also is fixed at 3cm for all lengths. For more details, about geometry see Table 1.

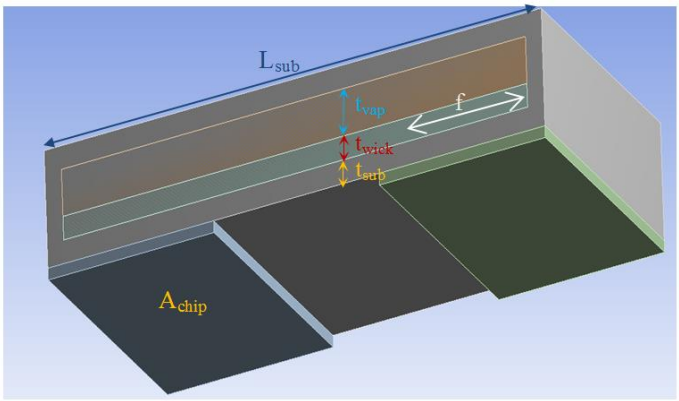


**Figure 4: Three dimensional cross sectional geometry for TGP.**

| | |
|---|---|
| $T_{cond}$=15˚C | $t_{wick}$ =0.33mm |
| ε=0.5 | $t_{vapor}$=0.67mm |
| $g_{factor}$=0 | $t_{sub}$= 1 mm |
| $L_{TGP}$ =30 mm | $d_{pore}$= 11.30 µm |
| $y_{ncg}$=0.1667 | $C_{sf}$=0.6 |
| $h_{evap}$= from Figure 7 | $h_{cond}$= from Figure 7 (7000 W/m$^2$.K) |

**Table 1: Input parameters.**

In order to estimate the equivalent thermal conductivity for the porous media (saturated liquid water filled the sintered copper wick). Maxwell [15] has presented an equation that offers the thermal conductivity of such a heterogeneous material:

$$k_{wick} = k_s\left[\frac{2+k_l/k_s-2.\varepsilon.(1-k_l/k_s)}{2+k_l/k_s+\varepsilon.(1-k_l/k_s)}\right] \quad (7)$$

Maxell's equation was validated by Laser flash method [16], using *Microflash* apparatus from Netzsch, which was used to measure the effective thermal conductivity of the porous wick. In this method, a laser pulse heats the sample from bottom while the thermal response is measured from the other side using an IR-detector. The transient thermal response is utilized to estimate the thermal diffusivity, which relates to the thermal conductivity of the sample. Samples were prepared by cutting out 8 mm x 8 mm x 1mm sections from a larger porous wick structure. Aluminum, copper and porous copper foam structures were used as reference baselines.

A total of 15 samples were tested three times to provide sufficient statistical data. Variation in measured effective thermal conductivity is attributed to local porosity variation within the sample [23]. As shown in Figure 5, the laser flash method gives an effective thermal conductivity of about 170 W/m.K for the sintered copper wick samples when the porosity about 0.5 and this is gives 4% error -related to the uncertainty of the wick porosity-when comparing with $k_{wick}$=163.2 W/m.K from Maxwell's equation. Since wick porosity is a factor in the equation, the model can also be used to predict the effect of wick porosity on TGP performance.

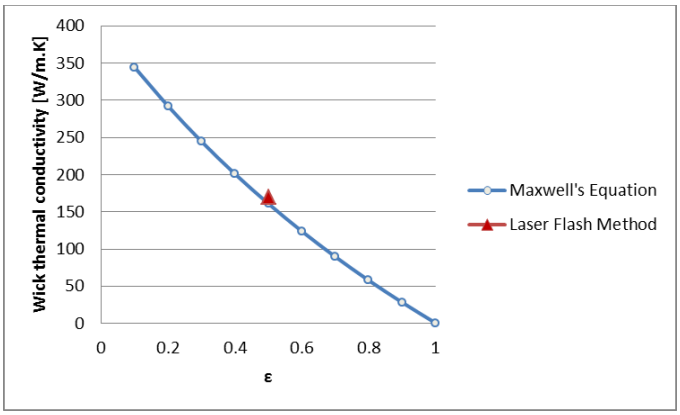


**Figure 5: Effective thermal conductivity of the wick samples as function of porosity.**

Several of the experimental work was implemented to measure wick performance as a function of evaporation rates for sintered copper wicks for modeling heat pipe. Iverson et al. [17] utilized a wick testing apparatus to compare the performance of different sintered wick samples of different porosity.

Nam et al. [18] reported the heat transfer performance of superhydrophilic Cu micropost wicks fabricated on thin silicon substrates utilizing electrochemical deposition and controlled chemical oxidation. Hanlon and Ma [19] introduced a 2D model to predict the overall heat transfer capability for a sintered wick and conducted an experimental study to predict the effective parameters for evaporation heat transfer from a sintered porous wick.

For the current work the thin film resistance at the interface was experimentally measured for the specific wick structures that were being fabricated. Figure 6 shows a schematic image of the setup for a 3cm open functional TGP, with 1cm heater, ε ~ 50%, pore diameter of 11.30 µm and about 0.5 mm wick thickness. The wick-substrate assembly is placed vertically in a fixture and heated at the top. The bottom of the sample is submerged in an ample supply of water, simulating a flooded or infinite condenser. In order to measure the evaporation limit and the evaporation resistance, the level of the water pool is adjusted so that only the heated area of the wick is exposed. This minimizes the uncertainty due to the effective area available for evaporation. In order to measure the capillary limit, the level of the water pool is adjusted to so as to vary the capillary length. The temperatures of the vapor and the water are

monitored to ensure that the chamber is maintained under saturation conditions. At the end of the test the liquid and vapor temperatures as well the chamber pressure is monitored to make sure that they return to the initial condition.

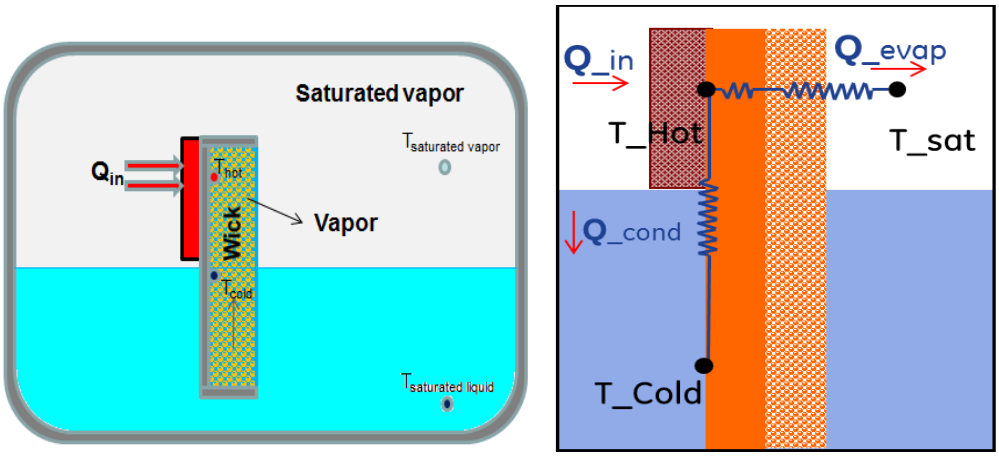


**Figure 6: Schematic of the experimental setup to measure evaporation heat transfer coefficient of wicks.**

The procedure to calculate the resistance at the evaporator is as follows. In general, some of the power supplied to the heater ($Q_{in}$) is conducted to the liquid pool ($Q_{cond}$) and the rest of it is convected ($Q_{conv}$) to the vapor through evaporation. The resistance network is shown in Figure 6. The conduction resistance ($R_{cond}$) to the liquid is measured by opening the chamber to atmospheric conditions. It is assumed that at this condition, for temperatures sufficiently below the evaporation temperature, $Q_{conv}$ is negligible. Once $R_{cond}$ is known, the heat conducted to the liquid ($Q_{cond}$) can be calculated using the temperature rise across the substrate. The internal resistance at the evaporator can be estimated using the following relation. In order to validate the assumption of neglecting $Q_{conv}$ and $Q_{cond}$, the amount of energy transported through evaporation ($Q_{evap}$) is found to be more than 95 percent out of the total energy ($Q_{in}$).

$$R_{Total} = \frac{(Q_{in} - Q_{cond})}{(T_{wall} - T_{vapor,sat})} - R_{substrate} \quad (8)$$

Where $T_{wall} \neq T_{vapor,sat}$ , it needs to be noted that in this calculation, $R_{Total}$ also contains the resistance through the wick ($R_{wick}$) and the resistance at the wick/substrate interface ($R_{wick\text{-}int}$). $R_{wick}$ and $R_{wick\text{-}int}$ can be measured using Laser Flash setup as mentioned before. Hence the phase change resistance at the evaporator ($R_{evap}$) can be obtained by:

$$R_{evap} = R_{Total} - R_{wick} - R_{wick-\text{int}} \quad (9)$$

From this resistance, the evaporation heat transfer coefficient can be calculated using:

$$h_{evap} = \frac{1}{R_{evap} A} \quad (10)$$

The setup was used to evaluate the effective heat transfer coefficient of uniform wicks. Experimentally measured $h_{evap}$ as a function of the temperature rise is shown in Figure 7, this curve will serve as a boundary condition in the TGP model. Notably, the thermocouples accuracy is evaluated as ± 0.78ºC. For more details about the uncertainty analysis, see reference [23].

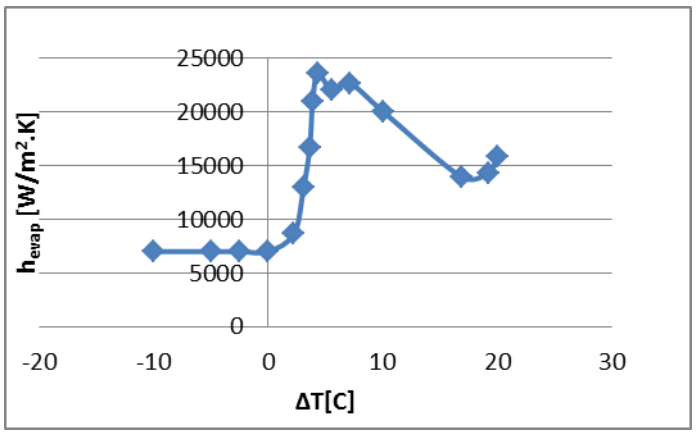


**Figure 7: Heat transfer coefficient as a function of ΔT.**

As for any heat pipe, for a TGP to work properly, the net capillary pressure difference between the wet and dry ends must be greater than the summation of all the pressure drop in the liquid and vapor flow.

$$\Delta P_{cap} = \Delta P_{liq} + \Delta P_{vap} + \Delta P_{body\,force} \quad (11)$$

The capillary pressure ($\Delta P_{cap}$) is given by Young-Laplace equation:

$$\Delta P_{cap} = C_1 \frac{2\sigma}{r_{pore}} \quad (12)$$

The $C_1$ value which is related to the contact angle and the standard deviation of average pore diameter is determined empirically, for different wick samples $C_1$ value is about 0.5.The capillary pressure can be experimentally evaluated by use of a so-called bubble point or bubble burst-through test. In this experiment a wicking sample is wetted and placed between an air reservoir and a reservoir with the working fluid reservoir [20]. In the experiment, the pressure of the air volume is then gradually increased to the point where bubbles appear in the liquid reservoir. At this point the pressure of the air reservoir has exceeded the meniscus pressure as air has been

able to penetrate the sample. Given known fluid properties, an effective pore radius can be evaluated. For the wick structures used in this study, the average pore diameter was found to be 11.30 µm. Further increasing the pressure and measuring the flow rate can also be used to evaluate the wick porosity.

The liquid pressure drop across the porous wick structure for laminar flows is approximated by:

$$\Delta P_{liq} = \frac{\dot{m}.\mu_l.L_{eff}}{K.\rho_l.A_{wick}} \quad (13)$$

The permeability (K) is used to evaluate the viscous pressure losses of transporting the working fluid through a section of the porous wicking structure. The pressure drop through the liquid channel is described by the Hagen–Poiseuille equation. This equation provides the pressure drop in a laminar, viscous and incompressible fluid flowing through a cylindrical tube. For an array of channels of circular cross-section pores in a wick of porosity of ε, the permeability of the wick is given by:

$$K = C_2 \frac{d_{pore}^2 \varepsilon}{32} \quad (14)$$

For Hagen-Poiseuille flow the constant $C_2$ is equal to 1, Where this value is determined experimentally from permeability test as shown in Figure 8 and equal to $C_2$=1.17. Also, from literature the permeability for the sintered metal powders is given by Chi equation:

$$K = \frac{r_p^2 \varepsilon^3}{37.5(1-\varepsilon)^2} \quad (15)$$

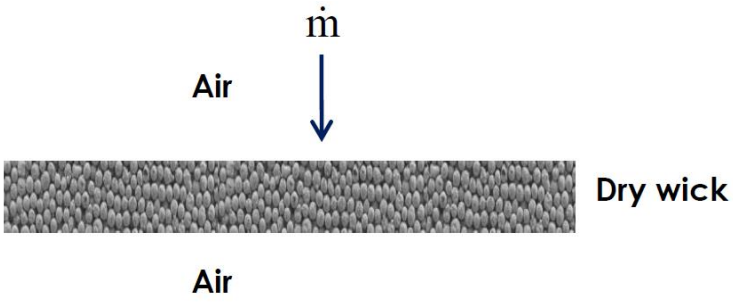


**Figure 8: Schematic of the permeability test.**

Figure 9 shows the relation between the pore size and permeability for the sintered wick. The pore size start from 1 µm to 100 µm at a constant porosity (ε =0.5). There was a strong agreement between measured K and permeability anticipated by the Hagen-Poiseuille equation. So this work demonstrates the shortcomings of this correlation (Eq.15) and suggested use of the Hagen-Poiseuille relation with a modified constant of 1.17 (Eq. 14) with improved success for this wick samples.

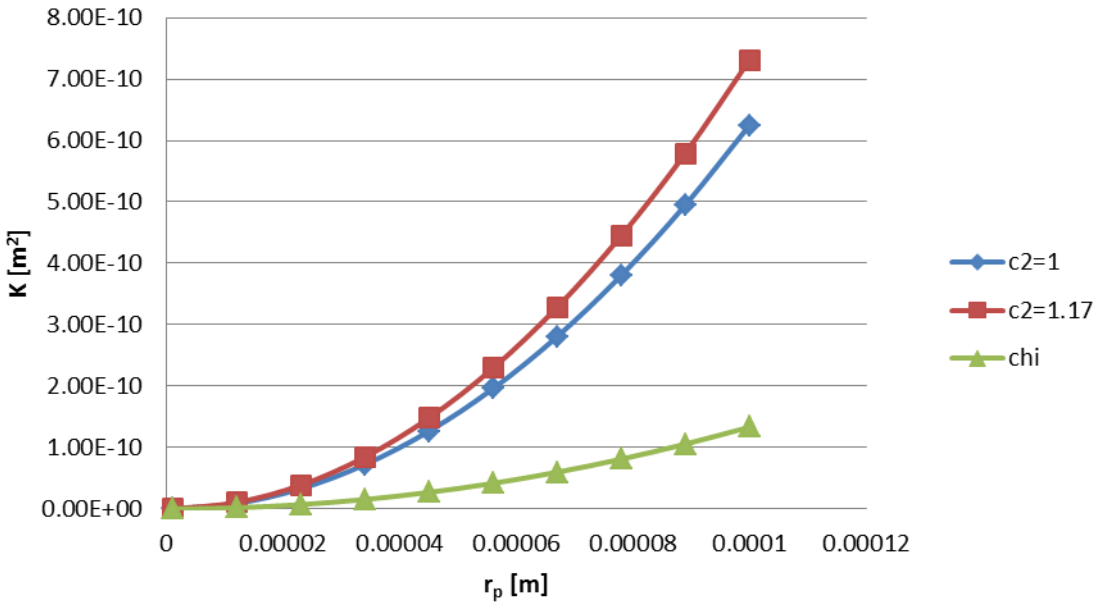


**Figure 9: Permeability as a function of the wick pore size.**

The vapor pressure drop across the vapor space for laminar flows is approximated by:

$$\Delta P_{vap} = \frac{32.\mu_v.L_{eff}.\dot{m}}{d_{vap}^2.\rho_v.A_{vap}} \quad (16)$$

Notably, $C_1$value, $C_2$ value, permeability (K) and the $h_{evap}$ curve are validated for a sintered copper wick with a thickness of 500µm, pore diameter of 11.30 µm and a porosity of 50%. Also, the effective length of the TGP which is denoted by $L_{eff}$ is equal to $L_{adiabtaic}+0.5(L_{evaporator} + L_{condenser})$.

Simple force equilibrium states that the wick structure can overcome 20-g acceleration if the capillary forces are stronger than the body forces. The gravitational forces working on the fluid can be demonstrated as a liquid column having a radius equal to the pore radius and length equal to the length of the TGP. To simulate the body forces that are a multiple of the gravitational acceleration g, this pressure is multiplied by a dimensionless factor ($g_{factor}$). The pressure related to this column can be defined as:

$$\Delta P_{bodyforce} = \rho_l.g.L_{TGP}.g_{factor} \quad (17)$$

The heat pipe heat load conveyed by the fluid is equivalent to the mass flow rate multiplied by the latent heat of vaporization.

$$Q_{HP} = \dot{m} h_{fg} \quad (18)$$

The effective thermal conductivity of the TGP is calculated using Equation 19:

$$k_{eff} = C_{sf} . Q_{HP} . \frac{L_{TGP}}{A_{TGP,cross} . \Delta T_{tot}} \quad (19)$$

The actual geometry and testing conditions are used as input parameters in the model. The parameters are listed in Table 1. The temperature rise across the TGP for a given heat input is calculated using the resistance values. The temperature rise is then used to estimate the equivalent thermal conductivity, $k_{eff}$, of the TGP. $k_{eff}$ is defined as the conductivity that a solid conductor would needs to have, if it were to have a similar thermal resistance

The heat transfer coefficients for evaporation as well as condensation are assumed to be an order of magnitude greater than the rest of the resistances, as a first-order approximation.

$C_{sf}$ is the shape factor, which is related to the thickness of the TGP. The shape factor value, approximately 0.6. $C_{sf}$, is presented to consider the effect for the two-dimensional heat flux pathway in the one dimensional equation [21] .For now, $Q_{HP}=Q_{TGP}$ because the axial heat fluxes on the wick and AlN are ignored. Eventually, to compare this thermo-fluid model with multi-dimensional model results, the axial heat fluxes will be considered.

The analysis calculates TGP temperatures and pressures using the EES software package [22]. Temperatures and pressures through the system are calculated using the equations, which are listed in the mathematical model section, for heat transfer areas, pressures, and thermodynamic properties in EES program with providing $Q_{in}$ and $T_{Condenser}$. Also, EES introduces a full review of heat transfer and pressures between the evaporator and condenser.

## RESULTS AND DISCUSSIONS

Figure 10 shows the effect of NCGs on the TGP thermal conductivity. It is clear that the TGP's thermal conductivity is proportional inversely to the mole fraction of NCGs. For the present testing arrangement, the condenser accounts for 33% of the whole TGP area as shown in the Figure 2 for $L_{TGP}$=3cm. As shown in the figure, when the entire condenser area is covered by NCGs, the performance drops to the baseline value. The three dashed lines represent a proposed amount of the NCGs in the TGP. It seems from the figure that the axial thermal conductivity of TGP reduces about 12% when the total volume fraction of NCGs is 0.07 and about 50% when the total volume fraction of NCGs is 0.23.Therefore, the entitlement of the TGP can be expected by this model, if the amount of NCGs are recognized.

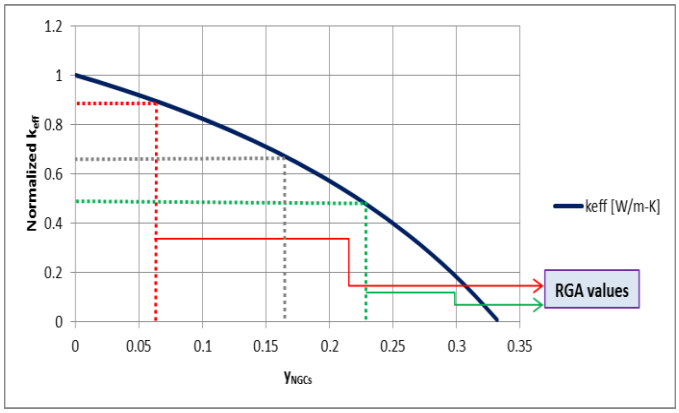


**Figure 10: Equivalent axial thermal conductivity as a function of mole fraction of NCGs.**

Figure 11 introduces the effect of the amount of NCG, which increases the chip temperature sharply if the condenser is blocked by NCGs, assuming that the condenser accounts for 33% of the whole TGP area. This trend is expected because the thermal resistance becomes infinity when the amount of (f) (percentage of NCGs that occupied the condenser side) approaches 1. Although this is an artifact of this model as it assumes all heat is transferred by two-phase heat transport, it illustrates the significant difficulty of operating a device with significant condenser blockage.

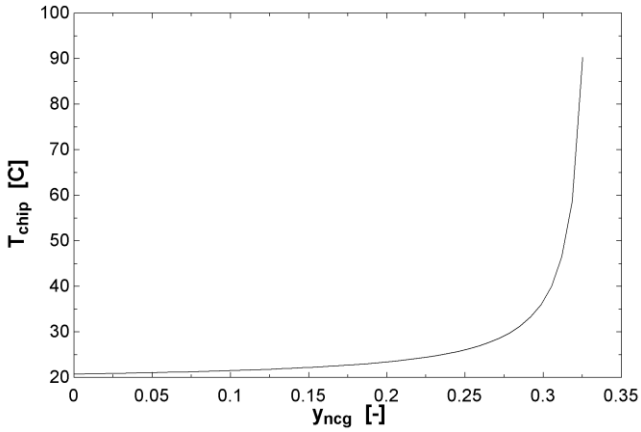


**Figure 11: TGP's chip temperature as a function of NCGs.**

Figure 12 shows the effect of the TGP's substrate thickness on its performance with NCGs ($y_{ncg}$=0.1667 or f =0.5) and without NCGs ($y_{ncg}$ =0.0) when $Q_{in}$ =30 W. It is obvious that when the substrate is thicker the axial thermal conductivity will decrease, because the thermal resistance will increase; the presence of NCG will decrease the $k_{eff}$ value too, due to an increase in the thermal resistance on the condenser side. Then the equivalent thermal resistance will be increased, too. The chip temperature increases with an

increase in the thickness of the substrate and with the presence of NCGs, because for the same heat input the increase of total thermal resistance will increase the chip temperature ($T_{chip}$) as well.

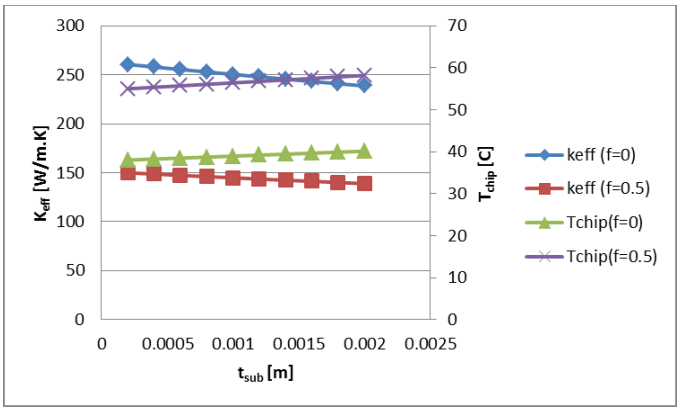


**Figure 12: Effect of substrate thickness and NCG fraction on TGP's performance.**

Figure 13 presents the performance of TGP as a function of wick thickness for a TGP with a 1 mm total thickness of the wick and the vapor space ($t_{wick}$+ $t_{vap}$=1mm) and without NCGs. The model was used to estimate the limits of wick thickness and vapor space thickness for a known internal volume so as to optimize the performance. The wick thickness is plotted on the x-axis where $k_{eff}$ and $Q_{max}$ are plotted on the left and right y-axis, respectively. It can be realized that at lower wick thicknesses, $Q_{max}$ is limited by the hydrodynamic losses in the wick. As the wick thickness increases, this loss decreases and increases $Q_{max}$. However, at a wick thickness of about 0.8 mm, the losses related to the vapor flow become significant and the flow becomes choked. As the vapor space is reduced, the velocity of vapor will be increased up to the speed of sound at which point it reaches the sonic limit. The effect of wick thickness is an important factor in designing the TGP. The maximum $k_{eff}$ value coincides with the $t_{wick}$ minimum (because the wick resistance is proportional to $t_{wick}$), but the maximum heat flux condition will not be met. The effect of doubling the wick thickness is a 20% reduction of the axial thermal conductivity of TGP in the wick thicknesses range (0.0001-0.0009m). Therefore, the upper and lower limits on the wick and vapor space thickness can be determined using this model.

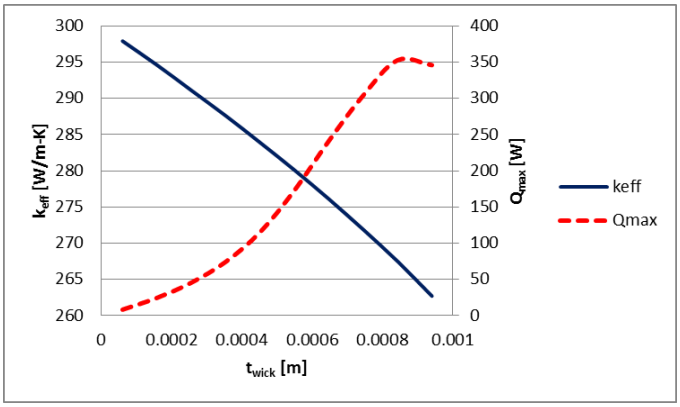


**Figure 13: Effect of wick thickness on TGP's performance.**

Figure 14 shows the effect of wick porosity on the TGP's performance. Effective thermal conductivity ($k_{eff}$) increases slightly with wick porosity (ε) until it approaches 0.6; then the trend of $k_{eff}$ starts decreasing by the increasing of (ε) because the void fraction plays a significant factor. This is mostly due to the lower thermal conductivity of water as compared with the sintered copper powder, which agrees mathematically with the experiment value for optimum wick porosity (ε≈0.55). On the other hand, increasing (ε) will increase the maximum heat flux ($Q_{max}$) because the wick with a higher porosity will have a lower pressure drop and consequently the mass flow through the system will be higher.

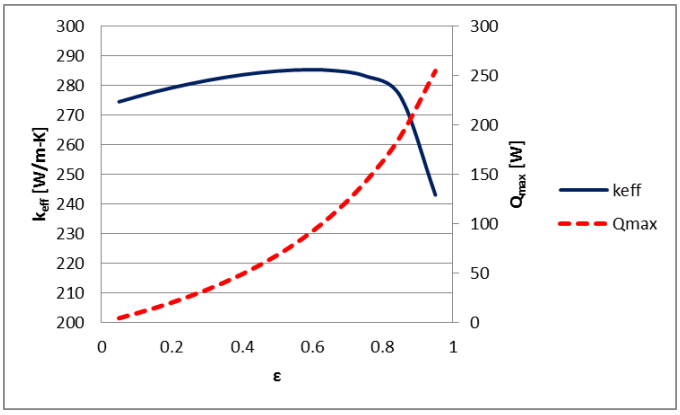


**Figure 14: Effect of wick porosity on the TGP's performance.**

Figure 15 gives the performance of TGP as a function of $g_{factor}$. As mentioned in the previous sections, it is expected that the gravity loading ($g_{factor}$) will have a strong influence on $Q_{max}$, while $k_{eff}$ will remain largely unaffected. It can be seen that a 20 'g' factor against the mass flow direction decreases the $Q_{max}$ by 60 %, from 72W to 29W. However, the $k_{eff}$ only increases by ~2%. Based on the wick parameters, it was observed that the TGP can transport >25W even with a 20 'g' factor acting against it.

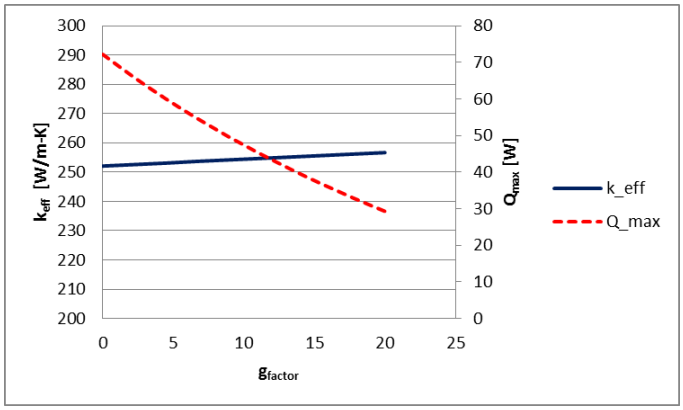


**Figure 15: Effect of gravitational acceleration factor on TGP's performance.**

Figure 16 shows a comparison between the model versus an experimental model. The experimental work was done for the high 'g' test at AFRL's spin table [21]. One of the key questions was to determine the effect of gravity loading on the TGP's performance. This test was performed at constant power (10W) [13]. It can be seen from Figure 14 that the effective thermal conductivity did not vary as a function of g-load; agreeing with the model, as effective thermal conductivity is based on the individual resistances of the components of the TGP as well as the heat transfer coefficients in the evaporator and condenser regions, which should change only slightly with high g-factor. Nevertheless, it is anticipated that the maximum heat transport capability decreases as the device is accelerated, as the capillary forces are opposed by the high-gravitational loading ($g_{factor}$), as shown in Figure 16.

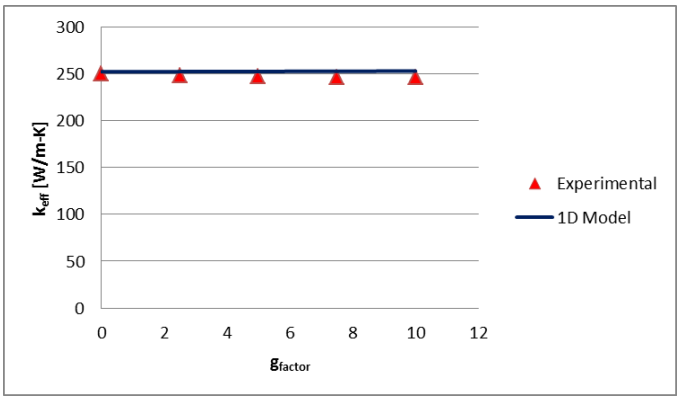


**Figure 16: Effect of gravitational acceleration factors on TGP's performance with constant input power Q=10W.**

Figure 17 shows the axial thermal conductivity for the TGP as a function of heat input for TGPs of differing length at $g_{factor}$ =1. It is obvious that $k_{eff}$ is sensitive to the heat input variation at same length. In the same way, $k_{eff}$ increases dramatically by 150% and 400% when the length changes from 3 cm to 9 cm and 15 cm, respectively. The figure shows for $L_{TGP}$=9 cm the capillary limit is

reached at Q ≈ 16 W, where the capillary limit is reached at Q ≈ 7 W when $L_{TGP}$ =15 cm, where for $L_{TGP}$ =3 cm the capillary limit will not exceed up to 50 W.

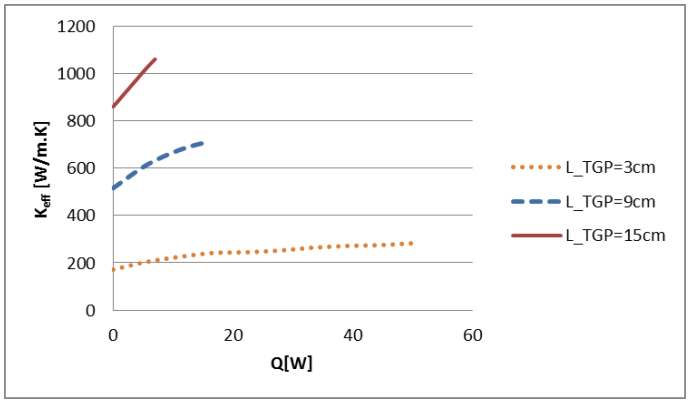


**Figure 17: Effect of heat input and the length on TGP's performance.**

The effect of the length of the TGPs on the performance at $g_{factor}$=1 is introduced in Figure 18. It is obvious that as the length of the TGPs increases, the effective axial thermal conductivity increases as addressed in equation 19. Also; a linear fitting for the normalized $k_{eff}$ as a function of TGP length is shown in the Figure. Figure 18 shows the value of the maximum axial length of the TGPs before reaching to the capillary limit. For example, for the same TGP if the power input 10 W, the maximum length before reaching to the capillary limit is about 11 cm. So, to prevent reaching the capillary limit rapidly, a graded wick by changing the configuration of variable $d_{pore}$ wick is the best solution to keep $k_{eff}$ increases as $L_{TGP}$ increases without reaching the capillary limit quickly ($Q_{max}$ will be enhanced).

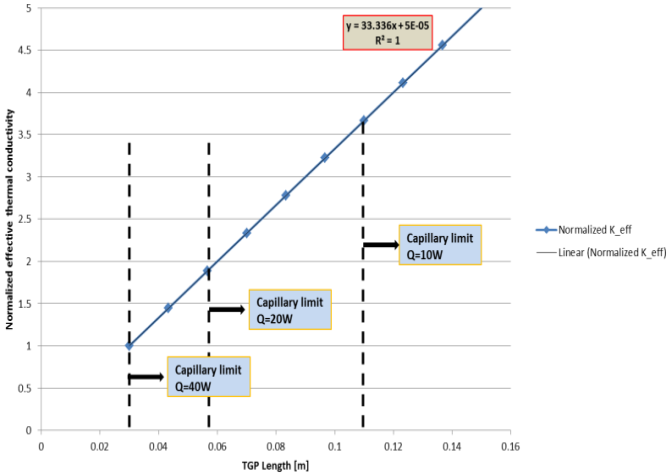


**Figure 18: Effect of TGP's length on their performance.**

Figure 19 shows maximum heat input of the TGP as a function of wick pore diameter at a different normalized wick thickness ($t_{wick}$*= $t_{wick}$/ ($t_{wick}$+$t_{vapor}$)) under $g_{factor}$=10 condition. It is clear that for the three different configurations of the normalized wick thicknesses ratios (10%, 50% and 90%), the 50% ratio is better than $t_{wick}$* = 10% and 90%. It is clear from the figure that at lower normalized wick thicknesses, $Q_{max}$ is limited by the hydrodynamic losses in the wick. As the normalized wick thickness increases, this loss decreases and increases $Q_{max}$. But at a normalized wick thickness of 90%, the losses related to the vapor flow become important. As the $t_{wick}$* is increased, the velocity of vapor will be increased up to the speed of sound at which point it reaches the sonic limit.

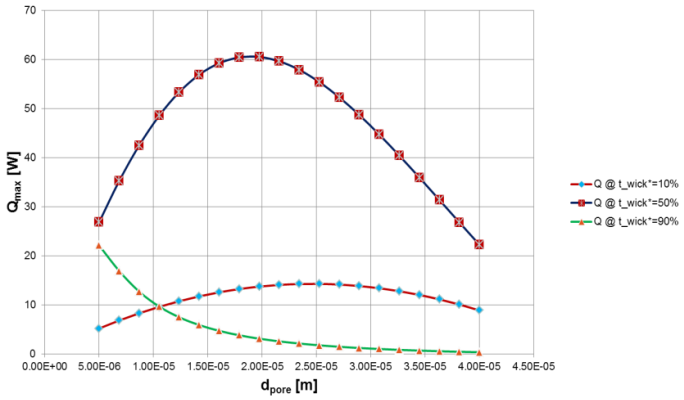


**Figure 19: TGP performance at $g_{factor}$=10.**

## CONCLUSIONS

The fundamental theory behind the transport of heat and mass in the TGP is an important issue so a thermal resistance model is developed to predict the performance of the TGP. A thermal resistance model is developed to predict the thermal performance of the TGP, including the effects of the presence of non-condensable gases (NCGs). Also, viscous laminar flow pressure losses are calculated to determine the maximum heat load when the capillary limit is reached.

The axial thermal conductivity of TGP reduces about 10% when the amount of NCGs on the condenser is 0.07 and about 50% when NCGs is 0.23. The axial effective thermal conductivity of the TGP decreases when the substrate is thicker and/or the presence of NCGs. The chip temperature increases with an increase in the thickness of the substrate and with the presence of NCGs. The model was used to optimize the performance of the TGP by estimating the limits of wick thickness and vapor space thickness for a known internal volume. The effect of wick thickness is an important factor in designing the TGP. The maximum $k_{eff}$ value coincides with the $t_{wick}$ minimum, but the maximum heat flux condition will not be met. In the existing range of the wick thickness the effect of doubling the wick thickness is a 20% reduction of the axial thermal conductivity of TGP. So, the optimum limits of the wick and vapor

space thickness can be estimated using this model. $k_{eff}$ increases slightly with (ε) until it approaches 0.6; then the trend of $k_{eff}$ starts decreasing by the increasing of (ε). On the other hand, increasing (ε) will increase the maximum heat flux ($Q_{max}$) because a wick with a higher porosity will have a lower pressure drop and consequently the mass flow through the system will be higher.

Increasing of 'g' factor will have a strong influence on decreasing $Q_{max}$, while $k_{eff}$ will stay largely unaffected. Also, to validate this result from the model, $k_{eff}$ is independent of 'g' factor; an experimental work was performed at a spin table. Also, this model can expect the capillary limit of the TGP based on pressure drop analysis. $k_{eff}$ increases by 150% and 400% when the length changes from 3 cm to 9 cm and 15 cm, respectively. But for $L_{TGP}$=9 cm the capillary limit is reached at Q ≈ 16 W, where the capillary limit is reached at Q ≈ 7 W when $L_{TGP}$ =15 cm. In conclusion, the maximum length of the TGP before reaching the capillary limit is inversely proportional with the $Q_{in}$. Finally, the optimum value for the wick thickness in the TGP is about $t_{wick}$* = 50% for three different configurations of wick thicknesses ratios (10%, 50% and 90%).

## ACKNOWLEDGMENTS

This paper is based upon work supported by DARPA under SSC SD Contract No. N66001-08-C-2008. Any opinions, findings and conclusions or recommendations expressed in this material are those of the author(s) and do not necessarily reflect the views of the SSC San Diego. Sincere appreciation is expressed to Stan Weaver for supplying the laser flash data and Professor Avram Bar-Cohen for his valuable comments.

## REFERENCES

1. Faghri, A., *Heat Pipe Science and Technology*, Taylor and Francis, Washington, DC, 1995.
2. Ababneh, M. T., Gerner, F. M., Hurd, D., De Bock, P., Chauhan, S., and Deng, T., "Charging Station of a Planar Miniature Thermal Ground Plane," Proceedings of the ASME/JSME 2011 8th Thermal Engineering Joint Conference, Honolulu, HI, 2011.
3. Kenny, T., 2007, "A–Thermal Ground Plane (TGP)," DARPA, Solicitation No. BAA07-36,1_darpa_baa07_36_tgp_final_for_posting_13apr07.pdf,https://www.fbo.gov/index?s= pportunity&mode=form&id=108cf5f7bcd8591d17b87082ec7b164a&tab=documents&tabmode=list
4. Ababneh, M.T., Chauhan, S.S. Gerner, F. M., Hurd, D., De Bock, P., and Deng, T., "Charging Station of a Planar Miniature Heat Pipe Thermal Ground Plane". J. Heat Transfer 135, 021401, 2013.

5. Ababneh, M.T., Gerner, F.M., Chamarthy, P., De Bock, P., Chauhan, S.S., and Deng, T., "Thermo-Fluid Model for High Thermal Conductivity Thermal Ground Planes" Proceedings of the ASME 2012 3rd Micro/Nanoscale Heat & Mass Transfer International Conference, Atlanta, GA, USA, March 3-6, 2012.
6. Ooijen, H., and Hoogendoorn, C. J., "Vapor flow calculations in a flat-plate heat pipe," AIAA Journal, 1979, 17, pp. 1251-1259.
7. Xiao, B., Faghri, A., "A three-dimensional thermal-fluid analysis of flat heat pipes," Int. J. Heat Mass Transfer 51: 2008, pp. 3113-3126.
8. Zaghdoudi, M.C., and Sarno, C., "Investigation on the effects of body force environment on flat heat pipes," J. Thermophysics and Heat Transfer, Vol. 15, No 4, 2001, pp. 384-394.
9. Thomas, S., and Yerkes, K., "Quasi-Steady-State Performance of a Heat Pipe Subjected to Transient Acceleration Loadings," AIAA Journal of Thermophysics, Vol. 11, No. 2, 1996, pp. 306-309.
10. Rice, J. and Faghri, A., "Analysis of Screen Wick Heat Pipes, Including Capillary Dry-out Limitations," AIAA Journal of Thermophysics and Heat Transfer, Vol. 21, No. 3, 2007, pp. 475-486.
11. Sonan, R., Harmand, S., Pelle, J., Leger, D., and Fakes, M., "Transient thermal and hydrodynamic model of flat heat pipe for the cooling of electronics components," Int. J. Heat Mass Transfer, 51: 2008, p.6006–6017.
12. Vadakkan U., Garimella S.V., Murthy J.Y., "Transport in flat heat pipes at high fluxes from multiple discrete sources," ASME J. Heat Transfer 126, 2004, pp.347–354.
13. De Bock,P., Chauhan,S., Chamarthy,P., et al., "On the Charging and Thermal Characterization of a micro/nano structured Thermal Ground Plane", Itherm 2010, Las Vegas, NV, USA, 2010.
14. Marcus, B.D., *Theory and Design of Variable Conductance Heat Pipes*, NASA CR-2018, April 1972.
15. Maxwell, J.C. "A treatise on electricity and magnetism," Vol. 1, 3rd Edn. OUP, 1954 (1981), reprinted by Dover, New York.
16. Netzsch *Microflash* equipment/setup description ( http://www.netzsch-thermal-analysis.com/us/products-solutions/thermal-diffusivity-conductivity/lfa-457-microflash.html).
17. Iverson, B.D., Davis, T.W., Garimella, S.V., North, M.T., Kang, S.S., "Heat and mass transport in heat pipe wick structures," J. Thermophys. Heat Transfer 21 (2), 2007, pp. 392–404.
18. Nam, Y., Sharratt, S., Cha, G.,and Ju, Y. S., "Characterization and Modeling of the Heat Transfer Performance of Nanostructured Cu Micropost Wicks" J. Heat Transfer, 2011, Vol. 133 / 10150.

19. Hanlon, M.A., and Ma, H.B., "Evaporation heat transfer in sintered porous media," J.Heat Transfer 34 (4), 2003, pp. 644–652.
20. De Bock, P., K. Varanasi, P. Chamarthy et al., "Experimental Investigation of Micro/Nano Heat Pipe Wick Structures", IMECE, October 31-November 6, 2008, Boston, Massachusetts, USA.
21. De Bock, P., et. al "Development and Experimental Validation of a Micro-Nano Thermal Ground Plane" Proceedings of the ASME/JSME 2011 8th Thermal Engineering Joint Conference, March 13-17, 2011, Honolulu, Hawaii, USA.
22. Klein, S.A., *Engineering Equation Solver*, Professional V8.157, F-Chart Software, 2008.
23. De Bock, P., 2013, *Design and Experimental Validation of a Micro-Nano Structured Thermal Ground Plane for High-g Environments*, Ph.D. Dissertation, University of Cincinnati.